Technical Physics, 2025, Vol. 70, No. 10

15

The principle of mechanical amplification for piezoelectric force sensors

© *A.P. Cherkun*

Institute of Spectroscopy, Russian Academy of Sciences,
108840 Troitsk, Moscow, Russia
e-mail: alexander.cherkun@yandex.ru

Received December 5, 2023
Revised June 9, 2025
Accepted July 6, 2025

In scanning probe microscopy (SPM), piezoelectric resonators (PR) are used to control the contact of the probe with the surface, the signal of the probe pressure force on the surface being directly converted into an electrical signal. The contact of the probe with the surface should occur through the contact of only single atoms. In order to increase sensitivity, a new technique for mechanical amplification of the force signal has been developed. The PR, combined with a primitive "dynamic amplifier" (DA) and a probe, form a new resonant system in which the amplitude of the vibrations of the PR is many times different from the amplitude of the vibrations of the probe. In this system, the DA serves as the first stage of amplification, and the PR as the second, so the output signal-to-noise ratio is determined by the noise of the first stage, which can be significantly less than the noise of the PR. Such system was carried out in practice with an experimental sensitivity of 1 pN scale in the 100 Hz frequency band, which is an order of magnitude better than the fundamental theoretical limit for PR without the use of DA. A detailed theoretical calculation of such a system is given.The described principle of mechanical amplification has a universal character and will allow using the same type of commercially available PR for different SPM tasks as well as for other types of diagnostics.

Keywords: probe microscopy, force noise, resonator, bending vibrations.

DOI: 10.61011/TP.2025.10.62095.298-23

Introduction

In 1995, the authors of [1,2] first reported that a clock quartz tuning fork (QTF), one of the types of piezoelectric resonators (PR), was successfully used in near-field scanning optical microscopy as a contact force sensor between the probe and surface. The same authors in [3], when examining the question regarding the smallest amplitudes that could be perceived by this type of sensors, pointed out that there was a noise force threshold $D_\mathrm{F} = 0.62\,\mathrm{pN}/\sqrt{\mathrm{Hz}}$ inherent in QTF employed by sensors operating in room atmosphere. However, an assumption that the minimum detectable force amplitude (MDF) at any QTF-based sensor design cannot be smaller than the noise threshold $F_\mathrm{min} = D_\mathrm{F}\sqrt{B}$, where B is a force signal frequency band [4], turns out to be wrong.

An equation for the noise threshold D_F is explicitly written in [5]:

$$D_\mathrm{F} = \sqrt{4K_\mathrm{B}T\gamma_\mathrm{eff}}\,(\mathrm{N}/\sqrt{\mathrm{Hz}}), \tag{1}$$

where γ_eff (N·s/m) is the effective viscous friction coefficient of oscillator; K_B is the Boltzmann constant; T is the temperature. When it comes to viscous air friction of QTF, then the smaller QTF the lower the viscosity and force noise. It is interesting that there is another noise reducing method. In [5], a sensor design is discussed (Figure 1, *b*) where not QTF, but small tip *5* of some „resonant console“ (RC), to which microscopic probe *2* is attached, has microscopic dimensions. It is also important that this tip oscillates with a much larger amplitude (Figure 1, *d*) than QTF arms *1*.

This RC being combined with QTF by drive *7* in a single oscillatory system turns out to serve as a dynamic amplifier of the force signal acting on the probe and is actually the first amplifying stage. Then the signal-to-noise ratio of the whole sensor is eventually defined by the first stage noise, i.e. according to (1) by the viscous friction coefficient of RC's microscopic tip 5. And this coefficient is approximately 100 times smaller than that of QTF. Consequently, the whole sensor, according to (1), turns out to be capable of perceiving 10 times smaller force amplitude than a traditional sensor (Figure 1, *a*) based on the same QTF.

Two sensor versions are shown schematically in Figure 1. Probe *2* has a microscopic pyramid shape with a height scale of 10 μm and a point radius of 10 nm. The QTF size scale is shown in the photo in Figure 1, *c*. The traditional sensor has QTF arm tips *1* oscillating at the resonance frequency of this QTF with an amplitude equal to the oscillation amplitude of probe *2*. When probe *2* approaches the surface of sample *4*, the probe is exposed to a variable pressure force at the same frequency. The purpose of the sensor and service electronics is to detect the amplitude of this force (the Fourier component amplitude is implied). The sensor attached to bearing console *11* performs horizontal line-by-line scanning of the sample *4*. During scanning, vertical movement of the sensor is included in the feedback loop to ensure a constant amplitude of the pressure force.

In contrast to the traditional sensor, the sensor with mechanical amplification in Figure 1, *b–d* had an experi-

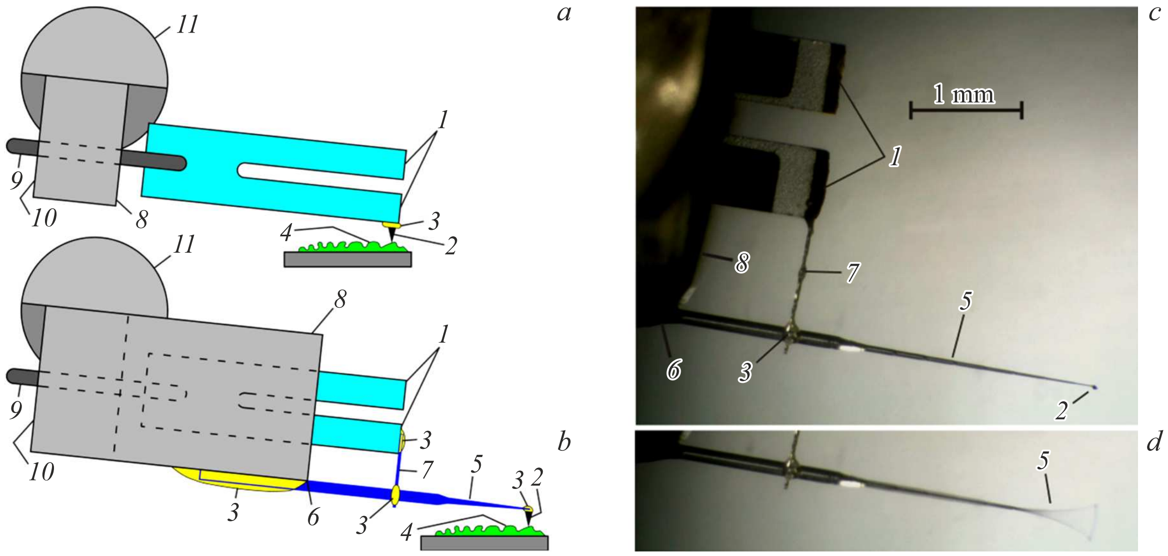

Figure 1. QTF-based contact sensors: *a* — a traditional sensor without an amplifier; *b* — with mechanical amplification; *c* — a photo of a real sensor; *d* — a photo of giant amplitude oscillations. *1* — QTF arms; *2* — a microscopic probe; *3* — adhesive bonding; *4* — a test sample; *5* — a resonant console and its tip; *6* — origin of the resonant console; *7* — connecting rod or drive; *8* — residual portion of the QTF's metal housing; *9* — QTF electrodes; *10* — QTF's glass base; *11* — sensor's bearing console.

mentally measured [5] oscillation amplitude of QTF arm tips *1* 33 times smaller than that of probe *2*. To demonstrate this fact in the photo, Figure 1, *d*, 10 V ac voltage was applied to QTF to induce a giant oscillation amplitude of probe *2*. During scanning, this amplitude is selected from a range from less than 1 nanometer to tens of nanometers.

Though seemingly simple as shown in photo, Figure 1, *c*, the design embodies several ideas and implements a number of practically important patterns. This variety of aspects may be compared with a complicated electric motor configuration, though it is actually an embodiment of Ampere's law. Finally, for the sensor used in [5] for magnetic force microscopy (MFM), the sensitivity or MDF $F_{\min} = 1.4$ pN at $B = 100$ Hz is reported. With such sensitivity, considering that two electrons spaced 10 nm apart repel each other with a force of 2.3 pN, an attempt may be made to „see“ single impurity atoms, donors or acceptors, on the semiconductor surface.

One of the first ideas of the configuration as shown in Figure 1, *b*, *c* is that RC *5* is bonded to QTF housing *8* in such a way that the natural resonance frequency of bending oscillations of its protruding part from point *6* to probe point *2* (drive *7* hasn't been bonded yet) is equal to the QTF resonance frequency. One of the key patterns is that the RC dynamic amplification factor is equal to the ratio of the oscillation amplitude of probe point *2* to the oscillation amplitude of the QTF arm rigidly bound to RC by drive *7*. Thus, this amplification in sensor [5] was equal to 33. Earlier in [6], this pattern has been verified experimentally. The above-mentioned amplitude ratio was equal there to 8, and in a subtle experiment with an electrostatic force, it was shown that the dynamic amplification produced by RC was also equal to 8 within 10 %.

This work provides theoretical description and justification of the set out aims and identified practical patterns that are important for successful development of a sensor with mechanical amplification (Figure 1, *b*, *c*). In particular, a full coefficient of conversion of the amplitude of a force acting on point *2* into the amplitude of electrical response on QTF electrodes *9* will be calculated. Noise, against which the effective signal was measured, will be also calculated. Though this is a calculation of a particular design, it may be simply modified for other projects. Another three application examples of the mechanical amplification principle for PR-based force sensors are given in the end of this paper.

1. Choosing the resonant console shape

For the purpose of MFM, increased force sensitivity with high force sensor response rate is required.

Figure 2, *a* shows the RC shape and dimensions chosen for this purpose. Dimensioning was performed empirically through numerical calculation of the RC bending resonance oscillation parameters corresponding to the current dimensions. The first aim of dimensioning is to ensure that the RC bending resonance oscillation frequency is equal to the QTF frequency. The second aim is large oscillation amplitude ratio of the tip and central part of RC. Other aims are simple shape, low „wind area or air caused viscosity “ of the tip, and low effective mass of the tip. Therefore, a shape in the form of a „long thin“ cone was chosen.

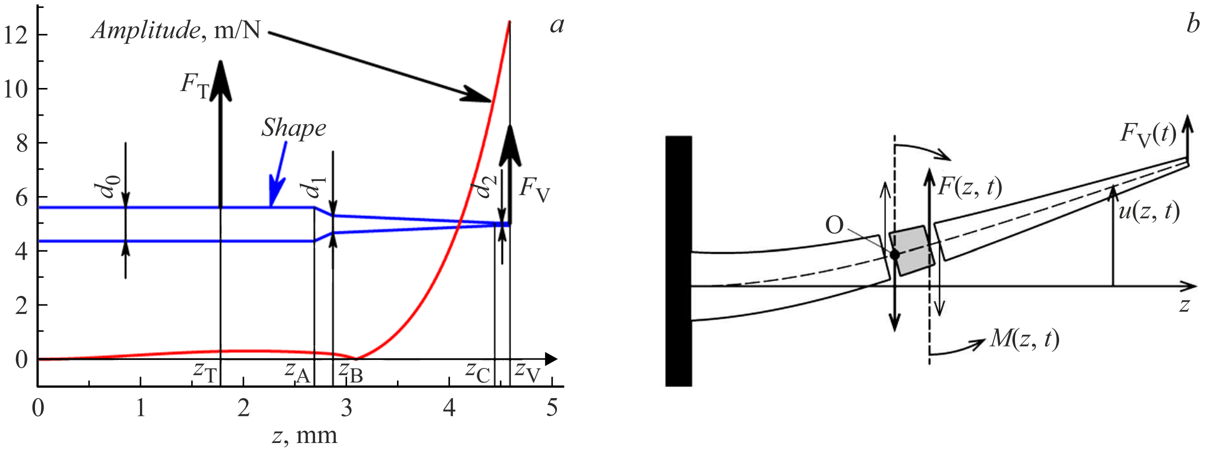

Figure 2. *a* — chosen RC shape and curve $|A(z)|$ of resonance oscillation amplitude distribution over the RC length z; *b* — diagram for a RC bending oscillation equation.

The initial diameter of RC $d_0 = 0.125$ mm corresponds to the standard diameter of the quartz optical fiber, from which RC is etched in fluoric acid. Then, at point $z_A = 2.69$ mm, significant diameter narrowing starts to $d_1 = 0.064$ mm at point $z_B = 2.87$ mm (the narrowing region is chosen in the form of a „short“ cone to satisfy the etching technique). Then, there is a „long“ cone to point $z_C = 4.44$ mm, within which the diameter decreases to $d_2 = 0.01$ mm. RC ends with a cylindrical portion $d_2 = 0.01$ mm (end point $z_V = 4.59$ mm). Narrowing from d_0 to d_1 is provided to reduce the RC effective mass that affects the sensor response rate. The „long“ conical portion, referred to as a „microrod“ in [5], serves to provide the largest oscillation amplitude of the RC tip with respect to the oscillation amplitude of the RC's „thick“ central portion at point $z_T = 1.78$ mm of the drive attachment. Conical shape is also important for reducing the RC effective mass and viscous air friction that is a force noise source and eventually defines the threshold force sensitivity of the sensor [5].

Figure 2, *a* also shows a calculated graph of the distribution of the amplitude modulus of resonant vibrations of such a RC (without drive 7) along its length, starting from the point $z = 0$ of the RC attachment (point *6* in Figure 1, *b, c*). There is an oscillation „node“ at point $z = 3.1$ mm. The nodes don't hinder operation, but RC may be elongated by adding nodes, if required. Design ratio of A_V at point z_V to A_T at point z_T appears to be quite significant: $K_0 = |A_V/A_T| = 42.66$. Then we show that a mechanical reinforcement with approximately the same K_0 occurs in RC by stating preliminary the exact meaning behind this concept.

2. RC oscillation equation and solution

To write the RC oscillation equation, a beam with length-varying diameter is shown in Figure 2, *b*. The left side of the beam is rigidly fixed. The straight axis z corresponds to the beam at rest, and beam center line displacement during small-amplitude bending oscillations is denoted by $u(z, t)$, where t is the time and z is the z axis coordinate. A thin beam is implied where the typical transverse dimension d is much smaller than the beam length l (for Figure 2, *a*, this corresponds to $d_0 \ll z_V$). The external force $F_V(t)$ acts on the free end, and the drive force $F_T(t)$ acts in the center at point $z = z_T$ as shown in Figure 2, *a*. A „small“ element is highlighted in grey and „thick“ lines show two transverse forces acting on this element from the rest part of the beam. Only one of them is denoted by $F(z, t)$. Also two rotational moments act on this component, one of which is denoted by $M(z, t)$. Bending oscillations in one plane are implied. The sum of moments with respect to point O is equal to

$$S_O = F(z, t)\Delta z + \frac{\partial M(z, t)}{\partial z}\Delta z = (F + M_z)\Delta z,$$

where Δz is the component length, and the „z“ or „t“ indices will hereinafter mean differentiation with respect to z or t. This sum causes the angular acceleration of the element according to the formula $S_O = (I\rho\Delta z)\varphi_{tt}$, where $I\rho\Delta z$ is the moment of inertia of the component with respect to O (at $\Delta z \ll d$); ρ is the density of material; I is the „moment of inertia of cross-section“, that for a round cross-section is $I = \pi d^4/64$; φ_{tt} is the angular acceleration, and φ is the angle according to $\varphi = \arctan(u_z) \approx u_z$. M at small oscillation amplitudes $u(z, t)$ is related to Young's modulus E of the material according to the known equation [2]:

$$M = u_{zz}EI. \tag{2}$$

It could be shown that for low-frequency resonance oscillation modes, $I\rho\varphi_{tt}$ has a square order of smallness $(d/l)^2$ with respect to M_z, and may be neglected for thin beams, i.e. $S_O = 0$, or

$$F = -M_z. \tag{3}$$

Newton's Law $F = ma$ written without external forces, for example, viscous air friction, will give $F_z = \rho s u_{tt}$, where

$s(z)$ is the current cross-section area. Now we add the viscosity:

$$F_z - gu_t = \rho s u_{tt}, \tag{4}$$

where $g(z)$ is the specific viscosity (N·s/m^2). For further calculations, we assume arbitrarily that for a round rod with the diameter $d(z)$ the specific viscosity is proportional to the diameter $g = \upsilon d$, and let $\upsilon = 100$ (N·s/m^3) (true viscosity and dependence on diameter are not relevant for demonstration purpose), for quartz optical fiber $\rho = 2659$ kg/m^3 and $E = 7.87 \cdot 10^{10}$ N/m^2 [2].

By substituting expressions (2), (3) and $s = \pi d^2/4$, $I = \pi d^4/64$, $g = \upsilon d$ for the round cross-section into equation (4), we get the following oscillation equation

$$(\pi d^2/4)\rho \cdot u_{tt} = -(\pi E/64) \cdot (d^4 u_{zz})_{zz} - \upsilon d u_t. \tag{5}$$

This is a homogeneous differential equation that is linear in $u(z, t)$ with variable (d depends on z) coefficients. But these coefficients are real and independent on t, therefore solutions may be sought for as

$$u(z, t) = \mathrm{real}[A(z) \exp(i\omega t)], \tag{6}$$

where „real" means the „real part", $A(z)$ is the complex amplitude, ω is the angular frequency. If the complex amplitude is written as $A(z) = |A(z)| \exp(i\varphi(z))$, then $u(z, t) = |A(z)| \cos(\omega t + \varphi(z))$. For acting forces, the following is similarly meant

$$g(z, t) = \mathrm{real}[F(z) \exp(i\omega t)] \text{ or } g_{\mathrm{V}}(t) = \mathrm{real}[F_{\mathrm{V}} \exp(i\omega t)].$$

Then after substituting $A(z) \exp(i\omega t)$ instead of $u(z, t)$ into (5), an ordinary differential equation is derived for the complex amplitude:

$$-\omega^2(\pi d^2/4)\rho \cdot A = -(\pi E/64)(d^4 A_{zz})_{zz} - i\omega\upsilon d \cdot A. \tag{7}$$

Boundary conditions for (7) at point $z = 0$: $A = 0$, $A_z = 0$; at point $z = z_{\mathrm{V}}$: $A_{zz} = 0$, $(\pi E/64)(d^4 A_{zz})_z = (-F_{\mathrm{V}})$ according to (3); with $z = z_{\mathrm{T}}$: A, A_z, A_{zz} are continuous, and $(\pi E/64)(d^4 A_{zz})_z$ has a jump $(+F_{\mathrm{T}})$. Equation (7) was solved numerically using the Runge–Kutta method for a set of fixed frequencies $f = \omega/(2\pi)$. It has two independent variables — force amplitudes F_{V} and F_{T}, and two main dependent variables — $A_{\mathrm{V}} = A(z_{\mathrm{V}})$ at z_{V} and $A_{\mathrm{T}} = A(z_{\mathrm{T}})$ at z_{T}.

One of the solutions is shown in Figure 2, *a*. This is the curve $|A(z)|$ of resonance amplitude distribution over the RC length at $F_{\mathrm{V}} = 1$ N, $F_{\mathrm{T}} = 0$, $f = 32768$ Hz. Simultaneously it may be considered that this is the RC oscillation amplitude module curve under the action of force with the amplitude $F_{\mathrm{T}} = K_0 \approx 42.66$ N with $F_{\mathrm{V}} = 0$, $f = 32768$ Hz, because the difference between these curves is not higher than 0.031 m/N, which is smaller than the curve line thickness.

RC dimensions were chosen in such a way that the RC resonance frequency was equal to the QTF resonance frequency $f_0 = 32768$, which is demonstrated on amplitude-frequency curve A_1 in Figure 3.

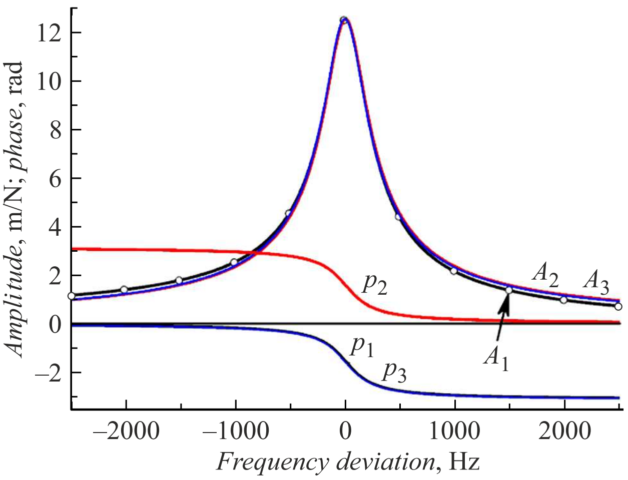

Figure 3. Calculated amplitude $A = |A(z_{\mathrm{V}})|$ and $p = \mathrm{imag}(\ln(A(z_{\mathrm{V}})))$ phase response of the RC tip to variable forces with the amplitude F_{V} or F_{T} acting on the tip or drive point depending on the frequency deviation $f - f_0$. A_1, p_1 — amplitude and phase at $F_{\mathrm{V}} = 1$ N and $F_{\mathrm{T}} = 0$; A_2, p_2 at $F_{\mathrm{V}} = 0$ and $F_{\mathrm{T}} = K_0 \approx 42.66$ N; A_3, p_3 amplitude and phase of classical oscillator with the effective mass m_{V}, viscosity coefficient γ_{V} and resonance frequency f_0 with $F_{\mathrm{V}} = 1$ N.

Curve A_2 looks almost the same — a 10% difference occurs only with deviation±1000 Hz, i.e. RC behaves alike when exposed to both F_{V} and $F_{\mathrm{T}} = K_0 F_{\mathrm{V}}$, which is K_0 times larger and is applied at $z = z_{\mathrm{T}}$, where the oscillation amplitude found from the curve in Figure 2, *a* is $K_0 \approx 42.66$ times smaller. Frequency dependences of the corresponding phases p_2 and p_1 differ by π rad (with an accuracy to two decimal places: $p_2 - p_1 = \pi \pm 0.03$ rad) due to the presence of oscillation „node" on the curve in Figure 2, *a*.

Effective mass m_{V} of RC oscillations reduced to the RC tip may be calculated by equating the corresponding kinetic oscillation energies:

$$m_{\mathrm{V}} = \left\{ \int_0^{z_{\mathrm{V}}} \rho s(z) |A(z)|^2 \partial z \right\} / |A(z_{\mathrm{V}})|^2. \tag{8}$$

The effective viscosity coefficient γ_{V} is calculated in the same way:

$$\gamma_{\mathrm{V}} = \left\{ \int_0^{z_{\mathrm{V}}} \upsilon d(z) |A(z)|^2 \partial z \right\} / |A(z_{\mathrm{V}})|^2. \tag{9}$$

Then, Figure 3 shows the accuracy with which the oscillation amplitude and phase of the classical oscillator according to

$$A_{\mathrm{V}} = F_{\mathrm{V}} / [m_{\mathrm{V}}(\omega_0^2 - \omega^2) + i\omega\gamma_{\mathrm{V}}]$$

coincide with curves A_1, p_1 for RC. If the effect of F_{T} is also considered, then the equation of this oscillator is written as

$$F_{\mathrm{V}} - F_{\mathrm{T}}/K_0 = m_{\mathrm{V}} \ddot{A}_{\mathrm{V}} + \gamma_{\mathrm{V}} \dot{A}_{\mathrm{V}} + k_{\mathrm{V}} A_{\mathrm{V}}, \tag{10}$$

where $k_V = \omega_0^2 m_V$; sign „–“ before F_T/K_0 considers that the drive point and RC tip oscillate in phase opposition (p_1 and p_2 in Figure 3).

It is interesting to note that an absolutely exact equality$A_1 = A_2$is achieved with $f - f_0 = 0$. This fact results from the general symmetry $A(x, y, f) = A(y, x, f)$ first found during numerical calculation where $A(z, z_1, f)$ denotes complex solution $A(z)$ of equation (7), when an external force with the amplitude $F = 1$ N and frequency f acts at point z_1(this is actually the delta function $\delta(z - z_1)$, and $A(z, z_1, f)$ is Green's function). Thus, for an equation of type (7), general „reciprocity principle“ first stated in the 19th century is satisfied. This is the principle where a single amplitude force acting at point $z = y$ at any f excites at point $z = x$ precisely the same (complex) oscillation amplitude as would have been excited at point $z = y$ by a single amplitude force acting at point $z = x$. In this terminology, $K_0 = |A(z_V, z_V, f_0)/A(z_T, z_V, f_0)|$ and $K_0 = |A(z_V, z_V, f_0)/A(z_V, z_T, f_0)|$ coincide. Conformity of the performed calculations to the reciprocity principle is a check for their correctness.

Calculated data in Figure 3 shows that RC behaves as a single oscillator mode in a broad frequency band $f_r \pm 500$ Hz, despite a quite long and thin tip $d_2 = 0.01$ mm. To be clear, the oscillation amplitude and phase in this frequency band or any point z behave in the same way as the amplitude and phase of the tip z_V in the curves in Figure 3, but for the amplitude at point z, the multiplier $|A(z)/A(z_V)|$ defined from the curve in Figure 2,*a* shall be considered. With a less favorable selection of RC shape, another RC resonance frequency could occur near f_0, which would have affected negatively the sensor response rate [4]. Calculation according to (8) gives $m_V = 1.62 \cdot 10^{-10}$ kg; effective dynamic stiffness coefficient $k_V = m_V \omega_0^2 = 6.85$ N/m; viscosity according to (9) $\gamma_V = 3.88 \cdot 10^{-7}$ N·s/m.

But for further objectives, it is convenient to represent the oscillator reflecting RC behavior within $f_r \pm 500$ Hz in terms of the drive point oscillations $z = z_T$, rather than in terms of the tip oscillations $z = z_V$. Then equation (10) will be written as:

$$F_T - K_0 F_V = m_T \ddot{A}_T + \gamma_T \dot{A}_T + k_T A_T, \tag{11}$$

where $m_T = K_0^2 m_V$; $\gamma_T = K_0^2 \gamma_V$; $k_T = \omega_0^2 m_T$; $A_V = -K_0 A_T$.

For explicit statement of the meaning behind the RC „amplification“ concept, a practice-related situation is considered [5,6], where some device „X“ supports a strictly constant oscillation amplitude $A_T = 1$ at point $z = z_T$, for example, at f_0. If at the tip $z = z_V$, ΔF_V starts acting at some frequency f, then, without device „X“ it would induce an additional oscillation amplitude $A(z_T, z_V, f)\Delta F_V$ at point z_T. But to keep the amplitude unchanged at point z_T, device „X“ will generate an additional force amplitude

$$\Delta F_T = -[A(z_T, z_V, f)/A(z_T, z_T, f)]\Delta F_V.$$

Then, considering the linearity of equation (5), the sum of additional amplitudes induced by ΔF_V and ΔF_T is exactly equal to 0 at point z_T. Calculation with $f = f_0$ gives $\Delta F_T \approx K_1 \exp(0.011i)\Delta F_V$, where the „amplification coefficient“ $K_1 \approx 42.63$ differs from K_0 only by 0.03, phase shift is about 0.011 rad. Within $f_0 \pm 500$ Hz, $K_1(f) = |-A(z_T, z_V, f)/A(z_T, z_T, f)|$ varies by max. 1.5, and the phase differs by max. 0.003 rad. This is one of the options to state and demonstrate RC's mechanical amplification and mechanical amplification deviation from K_0. For demonstration, mathematical analysis of equations could have been performed instead of numerical calculations and curves, but such approach currently seems superfluous. The following model will be used to show how the mechanical amplification works as part of a combined resonance system (CRS) consisting of RC and QTF connected by drive *7* Figure 1.

3. Complete electromechanical model of the sensor with mechanical amplification

Figure 4,*a* shows a diagram of QTF that has two arms with effective masses m_1 and m_2 and coordinates of motion of their tips x_1 and x_2 interconnected via a common crystal portion with effective mass m_3 that may rotate about some point O during bending of electrodes soldered to point O. For clarity, these rotational shifts are replaced by some generalized coordinate x_3. This simplified QTF diagram is shown in Figure 4,*b*, where each of three masses has

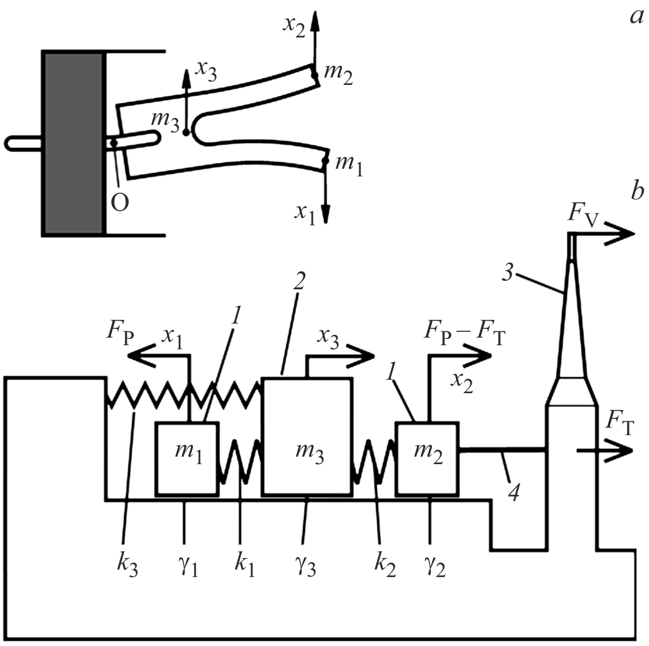

Figure 4. *a* — three main QTF components and their coordinates of motion; *b* — a CRS model where QTF is represented by three point masses and three coordinates of motion: *1* — QTF arms with masses m_1 and m_2 and coordinates x_1 and x_2; *2* — common crystal portion of the QTF arms with mass m_3 and coordinate x_3; *3* — RC as in Figure 2,*a*; *4* — drive.

its own viscous friction coefficient $\gamma_1, \gamma_2, \gamma_3$ and elastic couplings with stiffness coefficients k_1, k_2, k_3 as shown in the figure. Both arms are exposed to the same force F_P with equal value, but in opposite directions. The same two equal and opposite forces act on m_3 from m_1 and m_2. They are not shown because they sum to zero. Force from the drive $(-F_\mathrm{T})$ acts only on one arm m_2. The same force F_T with equal value, but opposite in direction, acts on RC via the drive as described above, and the force $F_\mathrm{V}$is applied.

Three Newton's equations of motion for three QTF model masses in Figure 4, *b* are:

$$\begin{gathered} m_2\ddot{x}_2 + \gamma_2\dot{x}_2 + k_2(x_2 - x_3) = F_\mathrm{P}(t) - F_\mathrm{T}(t), \\ m_1\ddot{x}_1 + \gamma_1(\dot{x})_1 + k_1(x_1 + x_3) = F_\mathrm{P}(t), \\ m_3\ddot{x}_3 + \gamma_3\dot{x}_3 + k_1(x_1 + x_3) + k_2(x_3 - x_2) + k_3x_3 = 0. \end{gathered} \tag{12}$$

Now equation (7) for RC is combined with system (12) for QTF using two equalities: equality of oscillation amplitudes $x_2 = A_\mathrm{T} = A(z_\mathrm{T})$ and equality of drive forces F_T. Some calculation results for this CRS are shown in Figure 5.

For calculation of curves in Figure 5, *a*, $m_1 = m_2 = m_0$ was assumed, where m_0 is the effective mass of one QTF arm according to equation (8), which for a constant-section beam is exactly equal to $m_0 = 0.25\rho V \approx 5.15 \cdot 10^{-7}$ kg, where $\rho = 2659\,\mathrm{kg/m^3}$ is the density, $V = 0.34 \cdot 0.6 \cdot 3.8 \cdot 10^{-9}\,\mathrm{m^3}$ is the arm volume; $k_1 = k_2 = \omega_0^2 m_0$; $\gamma_1 = \gamma_2 = \gamma_0 = \omega_0 m_0/Q$, where the Q factor $Q = 10\,000$; and $m_3 = 5m_0$, $k_3 = (5/9)k_2$, $\gamma_3 = 30\gamma_1$ are chosen arbitrarily. For this CRS, effective mass

$$m_\mathrm{S} = (2m_0 + K_0^2 m_\mathrm{V})/4 \tag{13}$$

and viscosity coefficient

$$\gamma_\mathrm{S} = (2\gamma_0 + K_0^2\gamma_\mathrm{V})/4. \tag{14}$$

are also calculated.

Calculation results in Figure 5, *a* show that CRS similar to RC within $f_r \pm 500$ Hz behaves as a single oscillator mode. Oscillation amplitude ratio of any two components of this oscillator with the specified frequency band is almost independent on frequency and this ratio is expressed in terms of K_0. Supplementary materials to [5] give an experimental curve of the RC tip oscillation amplitude and phase vs. the QTF electrode input voltage frequency. This curve corresponds to the behavior of A_4p_4 in Figure 5, *a*. Note that a quite accurate coincidence of A_7p_7 of the classical oscillator according to $A = F/[m_\mathrm{S}(\omega_0^2 - \omega^2) + i\omega\gamma_\mathrm{S}]$ at $F = K_0^2/4$ N with other CRS oscillation amplitudes and phases may be justified analytically. Substitution of the expression for F_T from (11) and of $x_2 = A_\mathrm{T}$ into system (12) provides above-mentioned expressions (13), (14) for m_S and γ_S. Notwithstanding that the RC effective mass m_V is 3200 times smaller than the arm mass m_0, $K_0^2 m_\mathrm{V}$ in (13) is not negligibly small any longer: $K_0^2 m_\mathrm{V} = 0.57m_0$. It is interesting to note that K_0 may be easily increased by several times without changing the RC shape. For this, the drive attachment point z_T shall be only moved closer to RC bonding point *6* (Figure 1), i.e. z_T shall be reduced. Then the CRS effective mass m_S will be several times greater than the initial QTF effective mass $m_0/2$, i.e. it will turn out that a small microrod will determine the effective mass of the whole CRS. Electrical inductance (15) of the sensor also grows, which will also slow down the sensor response rate [4]. In terms of the response rate and force sensitivity, m_V and γ_V shall be decreased and, therefore, the microrod dimensions shall be reduced. Figure 5, *a* shows that the amplitude in the deviation region $\Delta f = 2200$ Hz almost vanishes ($A_1 \approx 0.006$), and p_1 changes by π rad. With further reduction of the microrod dimensions, this Δf will decrease, which will limit the sensor's working frequency band. But the decrease in the working band will decrease the sensor response rate [4], i.e. selection of the optimum microrod size depends on the final target.

4. Coupling between CRS electrical and mechanical properties

Figure 6, *a* shows the equivalent circuit diagram of QTF that quite accurately describes its electrical properties within $f_r \pm 500$ Hz. This circuit together with equations expressing the coupling between the electrical circuit parameters and QTF's mechanical properties were frequently addressed in the literature [7]. For example, the inductance L_0 is proportional to m_0 of one QTF arm: $L_0 = m_0/(2\alpha^2)$, where α is the electromechanical coupling constant. From the experimental $L_0 = 5100$ H for QTF used in [5], $\alpha = 7.1 \cdot 10^{-6}$ N/V is calculated. Or the variable voltage generator amplitude $U_\mathrm{F} = F_\mathrm{T}/(2\alpha)$ is proportional to the variable force amplitude F_T acting on the QTF arm tip. These and many other equations may be derived from the illustrative diagram in Figure 6, *b*, where two L, R, C circuits are drawn in the transformer secondary circuit with conditional secondary-to-primary turn ratio $n_2/n_1 = \alpha$. These circuits represent two QTF arms and their inductances, resistances and capacities are directly expressed by mechanical parameters $m_1, \gamma_1, 1/k_1$ and $m_2, \gamma_2, 1/k_2$. Horizontal L, R, C bridge with $m_3, \gamma_3, 1/k_3$ represents coupling of two QTF arms through their common crystal portion, Figure 4. x_1, x_2, x_3 correspond to the displacements in Figure 4, but being reduced to the transformer primary winding, they will mean piezoelectric charges according to $q = \alpha x$. Then, current amplitudes will be $I = i\omega q = i\omega\alpha x$. The transformer secondary circuit diagram was chosen deliberately. It can be easily shown that the differential equations describing its behavior exactly coincide with equations (12) describing the behavior of three point masses m_1, m_2, m_3 in Figure 4. Just note that F_P will be expressed in (12) in terms of the voltage$U$ on the QTF electrodes as follows $F_\mathrm{P} = \alpha U$. Paper [8] evaluates the magnitude of α from the piezoelectric modulus $d_{21} = 2.31 \cdot 10^{-12}$ C/N for a quartz crystal. α depends on the shape of the

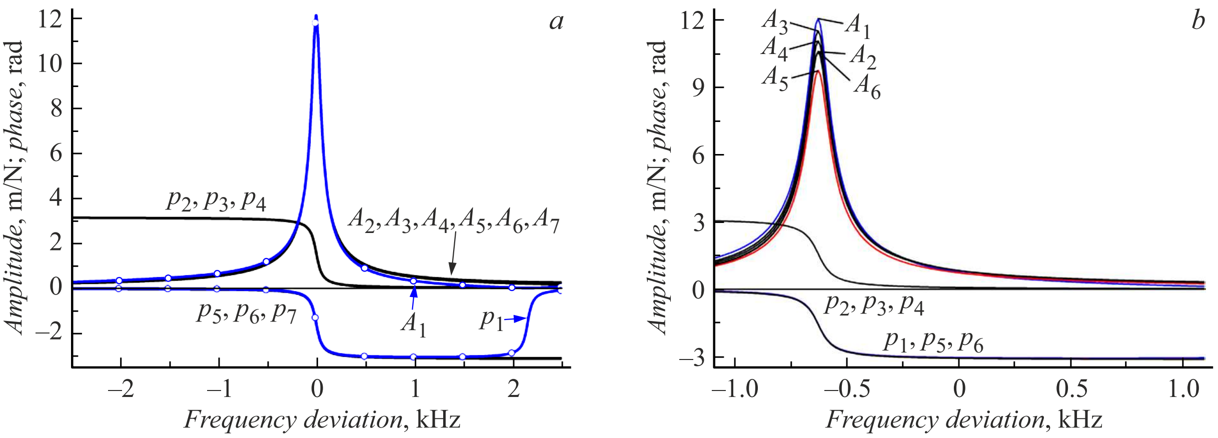

Figure 5. Calculated amplitude $|A(f)|$ and phase $p = \mathrm{imag}(\ln(A(f)))$ responses of the CRS components to variable forces with amplitudes F_V or F_P depending on $f - f_0$. a — when RC and QTF resonance frequencies coincide, when $m_1 = m_2 = m_0$; b — when RC and QTF frequencies differ by 2.5 %, when $m_2 = 1.1m_0$. A_1, p_1 — RC tip oscillation amplitude and phase at $F_V = 1$ N and $F_P = 0$; A_2, p_2 — amplitude and phase x_1 of the free QTF tip at $F_V = K_0$ N and $F_P = 0$; A_3, p_3 — amplitude and phase x_2 of the coupled QTF tip at $F_V = K_0$ N and $F_P = 0$; A_4, p_4 — that of RC tip at $F_V = 0$ and $F_P = K_0/2$ N; A_5, p_5 and A_6, p_6 — x_1 and x_2 at $F_V = 0$ and $F_P = K_0^2/2$ N; A_7, p_7 — amplitude and phase of the classical oscillator with m_S, γ_S and $f_r = f_0$ at $F = K_0^2/4$ N.

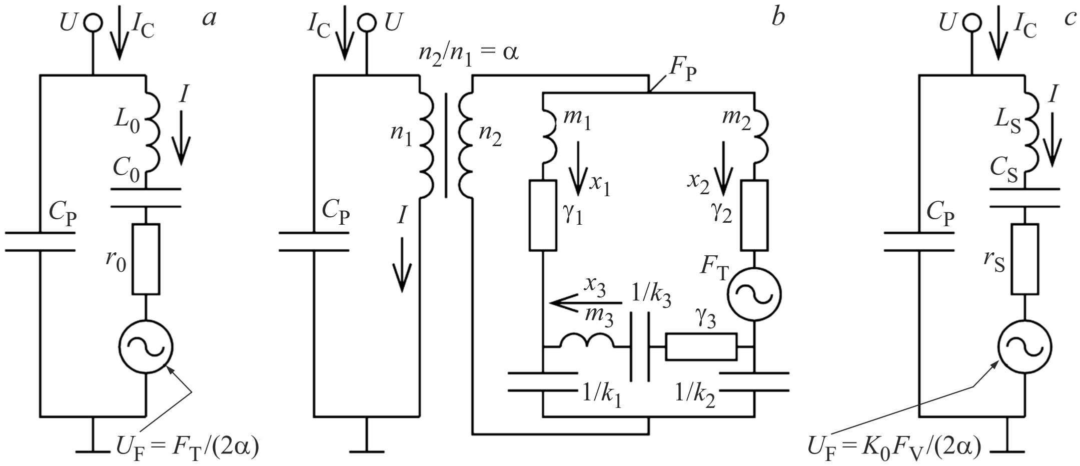

Figure 6. Three equivalent circuit diagrams: a — QTF circuit; b — model of two QTF arms and action of single electromechanical coupling constant α, where mechanical displacements x_1, x_2 are interpreted as electrical charges; c — circuit for CRS with mechanical amplification.

curve of oscillation amplitude distribution over the QTF arm length. Such curve is illustrated in Figure 2, a for RC. If the oscillation curve shape for each of two QTF arms changes slightly within $f_r \pm 500$ Hz, then it may be suggested that α is constant within these limits, which is implied in the circuits in Figure 6, b. The model in Figure 6, b probably will not accurately reflect all QTF behavior aspects when $m_1 = m_2$, $k_1 = k_2$, $\alpha_1 = \alpha_2$ are not satisfied, but it looks like the simplest and most reasonable from those models that would have been included all these parameters in. This model may be unambiguously calculated using both analytical and computerized tools.

One of the important results of these calculations is the conclusion that the electrical behavior of a complex CRS comes to the same simple equivalent diagram in Figure 6, c as the diagram in Figure 6, a. In this case, quite accurate expressions are derived for CRS inductance and resistance similar to (13) and (14):

$$L_S = (2m_0 + K_0^2 m_V)/(4\alpha^2), \tag{15}$$

$$r_S = (2\gamma_0 + K_0^2 \gamma_V)/(4\alpha^2). \tag{16}$$

Though curves A_7, p_7 in Figure 5 confirm only the efficiency of equations (13) and (14), and a series of experiments wasn't carried out to validate (15) and (16), nevertheless an increase in CRS inductance measured in a single experiment was $L_S/L_0 = 1.76$, and a calculation using (15) forecast an increase by 1.6 times. Considering the experiment error, correspondence of these two quantities is satisfactory.

The second important result is the demonstration of stable CRS behavior in the case when the equality of QTF and RC resonance frequencies is not accurately kept. For calculation of the curves in Figure 5, *b*, only one parameter was modified by 10 % compared with the calculation of the curves in Figure 5, *a* — $m_2 = 1.1m_0$was chosen. This reduces the QTF resonance frequency by 2.5 %, causes disbalance of two QTF arms and leads to a difference in the QTF and RC resonance frequencies by 2.5 %. In Figure 5, *b*, curves $A_1 - A_6$ and $p_1 - p_6$ have the same meaning as in Figure 5, *a*. It can be seen that CRS still behaves as a single oscillator mode. The amplitude equality of two QTF arms was maintained with a scale accuracy of 10 %, and the same high resonance oscillation amplitudes of the CRS components were maintained as in Figure 5, *a*. However, due to the small (10 %) difference that occurred between the QTF arm oscillation amplitudes, equations for L_{S} and r_{S} are now more complicated than (15) and (16). Note that the result shown in Figure 5 was not obvious a priori because CRS consists of many resonance components: two QTF arms plus RC with its microrod. A complex picture of closely spaced resonance frequencies could occur, or asymmetry induced by the drive bonded only to one QTF arm could lead to a great difference in the QTF arm oscillation amplitudes and currents flowing through the QTF arms.

It only remains to show that the mechanical amplification acts not only on RC, but also occurs as an electrical effect within CRS. In Figure 6, *c*, it concerns the voltage generator amplitude equation.

$$U_{\text{F}} = K_0 F_{\text{V}}/(2\alpha). \tag{17}$$

This generator expresses the CRS's electrical response to F_{V} acting on the RC tip. System of equations (12) together with equation (11) for RC are sufficient to show analytically how the following expression is derived

$$U - U_{\text{F}} = I\big(iwL_{\text{S}} + r_{\text{S}} + 1/(iwC_{\text{S}})\big).$$

And this equation being an analogue of Ohm's law for the right-hand equivalent circuit diagram in Figure 6, *c* will serve as justification of this circuit. Expressions for L_{S}, r_{S}, C_{S} and $U_{\text{F}} = K_0F_{\text{V}}/(2\alpha)$ were derived. Instead of this, we give a computer-aided calculation of the CRS application procedure as described in [5,6]. This procedure compensates the parallel capacitance C_{P} (Figure 6) ($C_{\text{P}} = 0$), and the current I is set to constant frequency and amplitude using a current generator, which results in constant oscillation amplitudes of the QTF arms and RC tip during scanning. ΔU on the QTF electrodes in response to ΔF_{V} acting on the RC tip serves as a measured variable.

Displacements x_1 and x_2 (Figure 4) are denoted by X_{P1} and X_{P2} in case of $F_{\text{P}} = 1$ and $F_{\text{V}} = 0$, and by X_{V1} and X_{V2} in case of $F_{\text{P}} = 0$ and $F_{\text{V}} = 1$. Considering $I = i\omega\alpha(x_1 + x_3 + x_2 - x_3) = i\omega\alpha(x_1 + x_2)$ and $\Delta F_{\text{P}} = \Delta U\alpha$, constancy of $\Delta I = 0$ may be written as

$$\Delta U\alpha(X_{\text{P1}} + X_{\text{P2}}) + \Delta F_{\text{V}}(X_{\text{V1}} + X_{\text{V2}}) = 0.$$

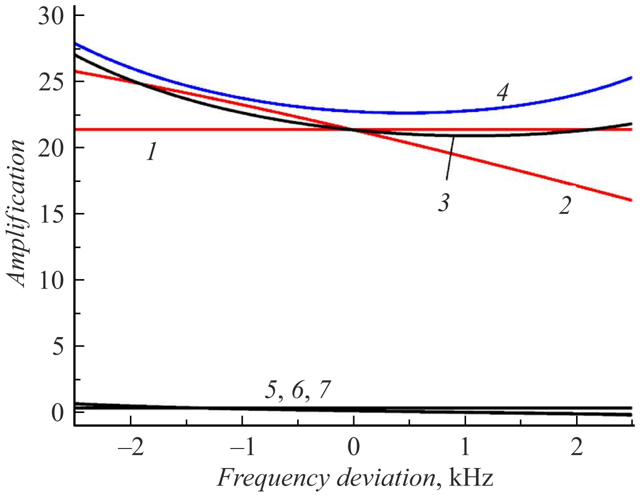

Figure 7. Amplification coefficient. *1* — $K_0/2$; *2* — $|G_{\text{K}}/2|$; *3* — $|G|$; *4* — the same $|G_{\text{dis}}|$ for disbalance $m_2 = 1.1m_0$; *5–7* — imaginary parts imag$(G_{\text{K}}/2)$, imag(G), imag(G_{dis}).

Figure 7 shows the extent to which the design amplification coefficient $G = -(X_{\text{V1}} + X_{\text{V2}})/(X_{\text{P1}} + X_{\text{P2}})$ differs from $K_0/2$ that corresponds to it in Figure 6, *c*. The figure also shows how the ratio $G_{\text{K}} = A(z_{\text{V}}, z_{\text{V}}, f)/A(z_{\text{T}}, z_{\text{V}}, f)$ of the amplitudes at points $z = z_{\text{V}}$ and $z = z_{\text{T}}$ depends on frequency for the free RC. The calculations were based on the solution to equation (7) together with system (12).

5. Evaluation of response rate and noise characteristics of a practically-implemented CRS

Now the equivalent diagram in Figure 6, *c* may be used to evaluate the response rate and noise characteristics of CRS as discussed in [5]. Figure 5 and 6 show that within $f_r \pm B$, where $B = 500\,\text{Hz}$, the amplitude and phase characteristics of CRS are qualitatively the same as those of QTF, therefore the CRS response rate will not differ from that of QTF according to the philosophy of [4], i.e. the response time is limited to $\tau > 1/(2\pi B) = 0.3\,\text{ms}$.

Force noise characteristics are defined by the viscous friction coefficients according to (1), but in [5] focus was made on the fact that the Johnson.Nyquist noise of the r_{S} resistor in Figure 6, *c* was the electrical expression of the force noise. Using (16), it may be immediately evaluated that CRS in the circuit diagram in Figure 6, *c* has the voltage noise threshold $D_{\text{U}} = \sqrt{4K_BTr_{\text{S}}}$ (V/$\sqrt{\text{Hz}}$) that according to (17) finally defines the sensor force noise threshold D_{FV}: $K_0D_{\text{FV}}/(2\alpha) = D_{\text{U}}$, i.e.

$$D_{\text{FV}} = \sqrt{4K_BTr_{\text{S}}} \cdot 2\alpha/K_0. \tag{18}$$

Substitution of experimental data from [5] $r_{\text{S}} = 900\,\text{k}\Omega$ and $K_0 = 33$ at $T = 300\,\text{K}$ gives $D_{\text{FV}} = 0.053\,\text{pN}/\sqrt{\text{Hz}}$, which is by an order of magnitude lower than

$D_F = 0.62\,\mathrm{pN}/\sqrt{\mathrm{Hz}}$ from [3] (in [5], similar QTFs with $D_F = \sqrt{4K_BTr_0}\cdot 2\alpha = 0.58\,\mathrm{pN}/\sqrt{\mathrm{Hz}}$ were used, where in room atmosphere $r_0 = 100\,\mathrm{k}\Omega$).

Let's get back to (16). If we break off the microrod tip, then r_S will drop to $r_S = 200\,\mathrm{k}\Omega$. This is an evidence that the „viscosity" of bonding *3* in Figure 1 increases $r_0 = 100\,\mathrm{k}\Omega$ by maximum two times. Therefore, the main contribution in equation (16) is made by $K_0^2\gamma_V$ and after substitution of this main part of (16) into (18) we get $D_{FV} = \sqrt{4K_BT\gamma_V}$, which is equivalent to (1). Moreover, according to equation (9), only a part of the microrod that oscillates with the largest amplitude as shown on curve, Figure 2, *a*, makes the main contribution to γ_V. The length of this part has a scale of 0.5 mm and is comparable with the cantilever length in the classical scanning probe microscopy (SPM), therefore the obtained noise threshold $D_{FV} = 0.053\,\mathrm{pN}/\sqrt{\mathrm{Hz}}$ has the same scale as the cantilever force noise in room atmosphere [5].

6. Mechanical amplification options

The above-mentioned philosophy and computational method may be used for developing other force sensor designs. Figure 8 shows several options.

Figure 8, *a* shows the way how the mechanical amplification could be used as part of the „qPlus" sensor [9]. Advantages offered by the „qPlus" sensor design, tiny dimensions and frequency modulation technique show up in solution of a wide range of SPM problems. Nevertheless, commercially-available cantilevers are by an order of magnitude smaller, therefore have lower force noise.

When arm *1* of the „qPlus" sensor is connect by light rigid push drive *2* to cantilever *3* in such a way that the distance from the cantilever and push drive to cantilever chip *4* is ≈ 6 times shorter than the cantilever length, then a ≈ 10-fold mechanical amplification of the force signal takes place. However, the other sensor properties, including the output force noise, will not much change and the signal-to-noise ratio will be up to 10 times better. Equality of the natural resonance frequencies of the cantilever and sensor is not required.

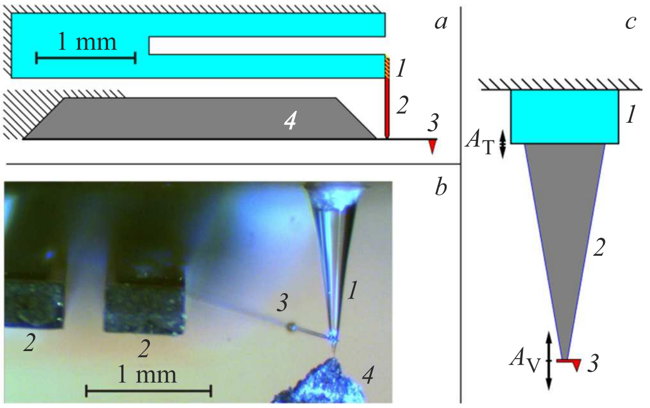

Figure 8. Mechanical amplification applications. *a* — as part of the „qPlus" sensor: *1* — the „qPlus sensor; *2* — the push drive; *3* — the commercially available cantilever with a probe (not to scale); *4* — cantilever chip. *b* — for operation with a rigid capillary probe: *1* — the capillary probe; *2* — the QTF arms; *3* — the drive; *4* — the sample, a Gd piece. *c* — amplification for longitudinal oscillations: *1* — PR; *2* — the amplifier body; *3* — the amplifier tip with the probe.

Paper [10] describes application of a conical quartz capillary with micron inlet as a probe. This capillary has a significant cone angle (Figure 8, *b*), therefore it has high mechanical rigidity and mass. The structure in Figure 8, *b* has no mechanical amplifier in the form of RC. Here, drive *3* is bonded to the center of the QTF arm, rather than to the QTF arm tip, and the QTF arm tip oscillation amplitude turns out to be $n \approx 3$ times larger than the capillary bending oscillation amplitude A_V in the capillary tip. Here, the mechanical amplification idea works backwards. Though, the force sensitivity formally decreases by $n \approx 3$ times, negative effect of the capillary rigidity on PR performance is reduced quadratically by $n^2 \approx 10$ times.

To increase the scanning rate, longitudinal oscillations may be used instead of bending oscillations when choosing the resonance frequency in the megahertz range. Figure 8, *c* shows a possible mechanical force amplification diagram in this case. The shape of mechanical amplifier body *2* shall be chosen such that the longitudinal resonance oscillation amplitude A_V of amplifier tip *3* is ≈ 10 times lager than the oscillation amplitude A_T of PR *1*. Amplifier *2* here plays a role of matching the microscopic dimensions and properties of the probe with those of PR.

Conclusion

When PR is used to measure the force acting on the probe tip in SPM, provisions can be made to ensure that A_T of PR differs from A_V of the probe tip by several times. Then $K = A_V/A_T$ becomes an additional design factor of the force sensor. By ensuring $K \gg 1$, the force signal may be increased by K times and the output signal-to-noise ratio may be improved at the same time. In case when $K \ll 1$, then, by loosing the sensitivity by $1/K$ times, the negative effect of the probe system rigidity or mass on PR may be decreased quadratically by $1/K^2$ times. When using a mechanical force amplifier in the form of a resonant console, then the amplification turns out to be low-noise and the sensor's signal-to-noise ratio may be improved by an order of magnitude. Finally, the force sensitivity achieves the level of the classical optical circuit in SPM, i.e. a sensor (Figure 1, *c*) with dimensions in the scale of 10 mm capable of operating in vacuum and at cryogenic temperatures replaces laser, two-element segmented photodiode and alignment mechanism. The sensor releases heat power less than 1 nW.

Conflict of interest

The author declares no conflict of interest.

References

[1] K. Karrai, R.D. Grober. Appl. Phys. Lett., **66**, 1842 (1995). https://doi.org/10.1063/1.113340

[2] K. Karrai, R.D. Grober. Ultramicroscopy, **61**, 197 (1995). https://doi.org/10.1016/0304-3991(95)00104

[3] R.D. Grober, J. Acimovic, J. Schuck, D. Hessman, P.J. Kindlemann, J. Hespanha, A.S. Morse, K. Karrai, I. Tiemann, S. Manus. Rev. Sci. Instrum., **71**, 2776 (2000). https://doi.org/10.1063/1.1150691

[4] D.V. Serebryakov, A.P. Cherkun, B.A. Loginov, V.S. Letokhov. Rev. Sci. Instrum., **73**, 1795 (2002). https://doi.org/10.1063/1.1462038

[5] A.P. Cherkun, G.V. Mishakov, A.V. Sharkov, E.I. Demikhov. Ultramicroscopy, **217**, 113072 (2020). https://doi.org/10.1016/j.ultramic.2020.113072

[6] A.P. Cherkun, D.V. Serebryakov, S.K. Sekatskii, I.V. Morozov, V.S. Letokhov. Rev. Sci. Instrum., **77**, 033703 (2006). https://doi.org/10.1063/1.2186386

[7] J. Rychen, T. Ihn, P. Studerus, A. Herrmann, K. Ensslin, H.J. Hug, P.J.A. van Schendel, H.J. Guntherodt. Rev. Sci. Instrum., **71**, 1695 (2000). https://doi.org/10.1063/1.1150521

[8] F.J. Giessibl. Appl. Phys. Lett., **76**, 1470 (2000). https://doi.org/10.1063/1.126067

[9] T. Seeholzer, D. Tarau, L. Hollendonner, A. Auer, R. Rachel, D. Grohmann, F.J. Giessibl, A.J. Weymouth. J. Phys. Chem. B, **127** (31), 6949 (2023). https://doi.org/10.1021/acs.jpcb.3c02875

[10] B.N. Mironov, S.A. Aseyev, S.V. Chekalin. Micron, **116**, 61 (2019). https://doi.org/10.1016/j.micron.2018.09.013

Translated by E.Ilinskaya